

## Current-driven domain wall motion in heterostructured ferromagnetic nanowires

Youngman Jang,<sup>a)</sup> Mark D. Mascaró, G. S. D. Beach, and C. A. Ross<sup>b)</sup>

Department of Materials Science and Engineering, Massachusetts Institute of Technology, Cambridge, Massachusetts 02139, USA

(Received 4 January 2012; accepted 14 February 2012; published online 12 March 2012)

Micromagnetic modeling shows that the placement of non-magnetic conductive pads on a ferromagnetic wire affects the current-induced velocity of a domain wall (DW) in the wire and can act as a DW chirality filter. The pads shunt the current, causing a non-uniform spin current distribution inside the ferromagnetic wire and an Oersted field transverse to the wire. This suppresses Walker breakdown allowing higher current densities to be imposed before breakdown occurs. The transverse Oersted field pins the DW under some regimes of current density and pad geometry, selectively allowing transmission of DWs of only one chirality. © 2012 American Institute of Physics. [<http://dx.doi.org/10.1063/1.3692797>]

The motion of magnetic domain walls (DWs) in geometrically confined magnetic wires is essential to the performance of information storage<sup>1,2</sup> and logic<sup>3,4</sup> devices, where a high and uniform DW velocity is required. DWs can be translated by a magnetic field, a spin-polarized current, or by a combination of the two. Considerable progress has been made in understanding field-driven domain wall motion in narrow magnetic stripes. The DW velocity is non-linear, increasing initially with increasing drive field to reach a value of typically several hundred m/s in NiFe (permalloy, or Py) stripes, but then decreasing abruptly above a critical field threshold. This Walker breakdown is accompanied by periodic transformations of the DW structure between a transverse and a vortex wall by the formation and annihilation of an antivortex core.<sup>5–8</sup> Various efforts have been made to prevent Walker breakdown.<sup>9–15</sup> In particular, the use of a comb-like structure was effective in suppressing field-driven Walker breakdown by periodically resetting the structure of the DW,<sup>14,15</sup> and provides a “chirality filter” effect in which transverse walls with opposite core magnetization have different propagation fields.<sup>15</sup>

Similarly to the field-driven case, current-driven DWs can exhibit breakdown-like behavior beyond a critical spin current density. Current-induced magnetization dynamics can be described by the phenomenological Landau-Lifshitz-Gilbert (LLG) equation<sup>16,17</sup>

$$\begin{aligned} \partial \mathbf{M} / \partial t = & \gamma \mathbf{H}_{\text{eff}} \times \mathbf{M} + \alpha / M_S (\mathbf{M} \times \partial \mathbf{M} / \partial t) - (u \cdot \nabla) \mathbf{M} \\ & + \beta / M_S [\mathbf{M} \times (u \cdot \nabla) \mathbf{M}], \end{aligned} \quad (1)$$

where  $\gamma$  is the gyromagnetic ratio,  $\alpha$  is the Gilbert damping constant,  $M_S$  is the saturation magnetization, and  $\mathbf{H}_{\text{eff}}$  is the effective magnetic field consisting of external, anisotropy, exchange, and magnetostatic fields. The term  $u (=PJ_e\mu_B/eM_S)$

represents the magnitude of the spin current density, where  $P$  is the spin polarization,  $J_e$  is the current density, and  $\beta$  parameterizes the nonadiabatic spin torque, which is related to spin relaxation or momentum transfer. Although the magnitude of  $\beta$  is predicted to be of the order of the damping constant  $\alpha$ , its value is still controversial.<sup>18–23</sup> Values of  $\beta = \alpha$ ,<sup>1</sup>  $\beta = 8\alpha$ ,<sup>21,23</sup> and  $\beta = 15\alpha$ <sup>19</sup> have been suggested for permalloy. While the last two terms in the LLG equation describe current-induced DW motion, they also predict a distortion of the DW structure whenever  $\beta \neq \alpha$ . In particular, the non-adiabatic spin torque term is responsible for an out-of-plane torque, resulting in a periodic transformation between transverse and vortex DW configurations at a critical value of  $u$  proportional to  $1/|\beta - \alpha|$ , and a drop in velocity if  $\beta > \alpha$ .<sup>16</sup>

The majority of studies of current-driven DW motion has considered the case of combined field and current parallel to the stripe in order to reduce the current densities needed to translate the DW. However, in “racetrack” devices based on the movement of multiple DWs, it is necessary to translate both head-to-head and tail-to-tail DWs with the same velocity. A scheme based on spin current without an applied field is, therefore, attractive, and there has been both experimental and computational work<sup>1,16,18,19,24</sup> on DW motion driven by current alone. However, there has been little work directed towards stabilizing DWs against current-induced torques, nor on methods for chirality filtering in current-driven DW motion.

This article describes modeling results for current-driven DW motion in a straight-edged magnetic stripe with overlaid non-magnetic current-shunting pads that give a periodic modulation in the magnitude of the spin current. The DW motion was computed by numerical solution of Eq. (1) using the object oriented micromagnetic framework (OOMMF).<sup>25</sup> The model consists of a Py nanowire 10  $\mu\text{m}$  long with a rectangular cross section 140 nm wide and 10 nm thick. The dimensions of the unit cells were  $5 \times 5 \times 10 \text{ nm}^3$ , such that the wire was one unit cell thick. The saturation magnetization  $M_S$  was 800 emu/cm<sup>3</sup>, exchange stiffness constant  $A = 1.3 \times 10^{-6} \text{ erg/cm}$ , damping constant  $\alpha = 0.02$ , and magnetocrystalline anisotropy = 0, and there were no extrinsic pinning sites. A value for  $\beta = 5\alpha$  was taken to give

<sup>a)</sup>Present address: Samsung Advanced Institute of Technology, Giheung-gu, Yongin, Gyeonggi-do 449-712, Korea. Electronic mail: youngman.jang@samsung.com.

<sup>b)</sup>Author to whom correspondence should be addressed. Electronic mail: caross@mit.edu.

breakdown at a moderate value of  $u$ . In this geometry,  $180^\circ$  transverse DWs with length of  $\sim 120$  nm were formed as the ground state boundary between domains magnetized parallel to the wire.

The spin current was modulated by adding current-shunting Au pads of 40 nm thickness onto the Py nanowire, labeled Type I in Fig. 1(a). In this structure, the effects of Oersted field were minimized by placing Au layers symmetrically both above and underneath the Py nanowire. The additional influence of a periodic transverse Oersted field was investigated using an asymmetrical structure, Type II, in which 10 nm Au pads overlaid the top of the Py nanowire. The resistivity for the 10 nm thick Au layer, 40 nm thick Au layer, and 10 nm thick Py layer was taken as 12, 5, and  $42 \mu\Omega$  cm, respectively.<sup>26,27</sup> Different lengths of the Au pads ( $l_{Au}$ ) ranging from 100 nm to 300 nm and different lengths of the Py separating the Au pads ( $l_{Py}$ ) ranging from 150 nm to 1350 nm were modeled.

Figs. 1(b) and 1(c) show the current distribution and the Oersted field calculated using a finite element model with 10 nm cell sizes for the part of the wire covered by the Au pads, in the case where the uncovered Py regions supported a current density of  $7.14 \times 10^8$  A/cm<sup>2</sup>, corresponding to a spin current velocity of  $u = 200$  m/s. The Au pads shunted the current and  $u$  decreased to 2.5 m/s in the Py under the Au for

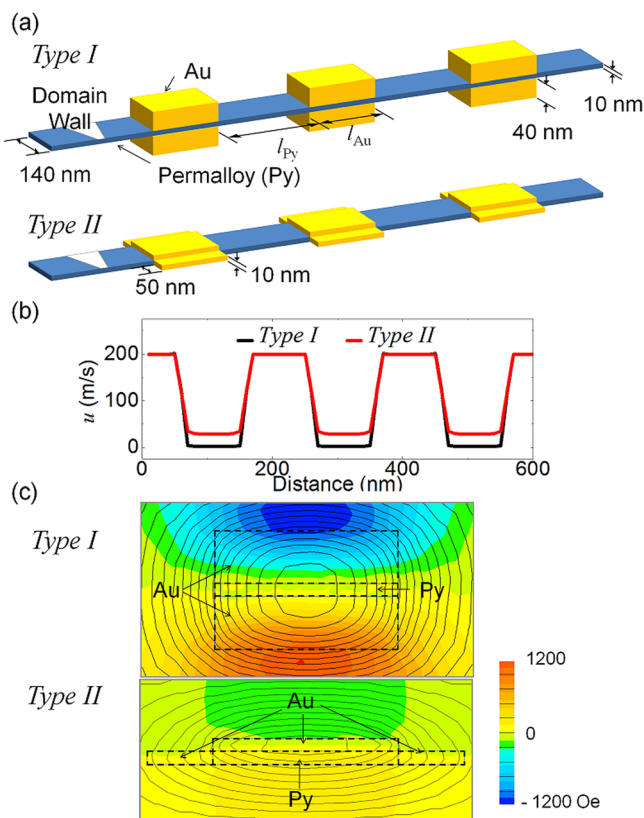


FIG. 1. (Color online) (a) Geometries of Py nanowires, 10 nm thick and 140 nm wide, with Au layers 40 nm thick (Type I) and 10 nm thick (Type II). In Type I, the Au layers are present above and underneath the Py nanowire to minimise the Oersted field. Type II has Au on the top of the wire and a transverse Oersted field is therefore generated inside the Py nanowire. (b) Current distribution at  $l_{Au} = 100$  nm for a spin current velocity  $u$  of 200 m/s in the uncovered part of the wire. (c) Oersted field in Py covered by Au pads when  $u = 200$  m/s in the uncovered part of the wire.

Type I geometry, and 28.5 m/s for Type II. Fig. 1(c) shows the Oersted field distribution at the cross section of an Au/Py region. The Oersted field in the Py was negligible for Type I but it reached 166 Oe in the transverse in-plane direction in Type II.

To provide a comparison with the heterostructured wires, we first model current-driven DW motion at zero applied field in an unpatterned Py nanowire without Au pads. Fig. 2(a) shows the time dependence of the DW velocity  $v$  for  $u = 130$  m/s, 160 m/s and, 200 m/s. The  $u = 130$  m/s case was below the Walker breakdown threshold of 140 m/s, and the DW velocity increased monotonically until it reached a value of 643 m/s after 8 ns, in agreement with the steady state value of  $v = \beta u / \alpha = 650$  m/s expected below breakdown.<sup>16</sup> Values of  $u = 160$  m/s and 200 m/s were above the Walker limit, and the DW velocity fluctuated periodically between positive and negative values. The drop in velocity immediately following the maximum velocity corresponded to the appearance of an antivortex core at the edge of the wire which initiated the transformation of the DW structure.

In contrast, Fig. 2(b) shows DW velocity  $v$  for the Type I structure (no Oersted field) when the length of uncovered Py was  $l_{Py} = 300$  nm and the length of the Au pad was  $l_{Au} = 100$  nm, 150 nm, 200 nm, and 250 nm, with  $u = 200$  m/s in the uncovered part of the wire. The  $l_{Au} = 100$  nm case exhibited Walker breakdown, though the wall was translated through  $\sim 1000$  nm before the breakdown initiated (in comparison, breakdown initiated in the unpatterned wire after  $\sim 600$  nm at  $u = 200$  m/s). In contrast, for the other values of  $u$ ,  $v$  fluctuated periodically over a distance of  $l_{Au} + l_{Py}$  but remained positive, with  $l_{Au} = 150$  nm giving the highest average velocity. Fig. 2(c) shows the DW displacement vs. time at  $u = 200$  m/s for the unpatterned Py nanowire compared to the Type I structure with  $l_{Py} = 300$  nm and  $l_{Au} = 150$  nm. The average DW velocity  $\langle v \rangle$  was doubled from 298 m/s to 605 m/s, and the fluctuations in velocity shown in the inset are considerably reduced for the wire with the Au pads.

The internal structure of the moving DWs for  $u = 200$  m/s is shown in Fig. 2(d) for the unpatterned nanowire and in Fig. 2(e) for the wire with pads. As in the case of field-driven DWs, the unpatterned wire in Fig. 2(d) exhibited nucleation of an antivortex core which traversed the width of the wire to reverse the magnetization direction within the core of the DW. This process was repeated in the next cycle by nucleation of an antivortex at the other side of the wire with opposite out-of-plane component and direction of transverse motion. In contrast, the DW in the Type I Py nanowire, Fig. 2(e), maintained its structure. Even though the DW velocity in the Au-covered regions was reduced, the retrograde motion was suppressed and the average velocity was enhanced because the reduction in  $u$  under the pads impeded the formation and movement of the antivortex.

The relation between  $\langle v \rangle$ ,  $u$ , and  $l_{Py}$  is mapped in Fig. 3(a) for  $l_{Au} = 150$  nm. The  $\langle v \rangle$  was averaged for DW motion over a distance of  $4 \mu\text{m}$ . The top panel shows the data for the unpatterned wire on the same scale. The data points for Fig. 3 were extracted from a set of calculations with intervals of 20 m/s in  $u$  and 40–60 nm in  $l_{Py}$ , and discretized into color

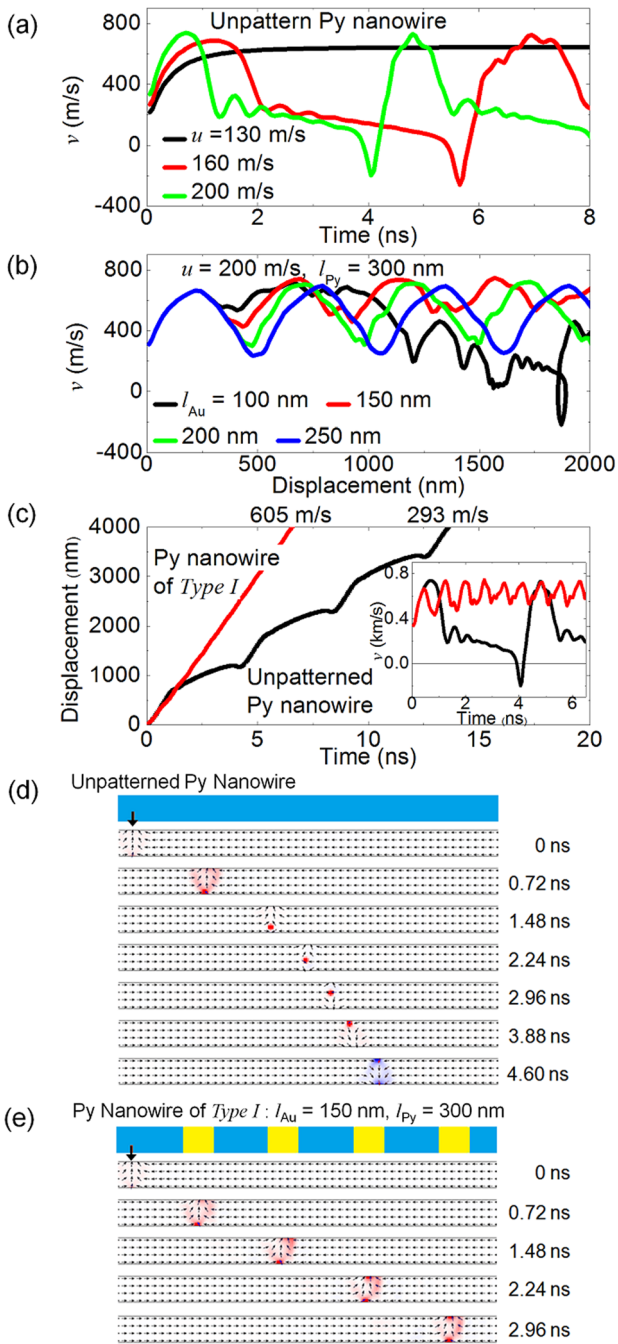


FIG. 2. (Color online) (a) DW velocity  $v$  as a function of time for  $u = 130$  m/s, 160 m/s, and 200 m/s in the unpatterned Py nanowire. (b)  $v$  in terms of the DW displacement for  $l_{Au} = 100$  nm, 150 nm, 200 nm, and 250 nm. (c) DW displacement in terms of time at  $u = 200$  m/s,  $l_{Py} = 300$  nm, and  $l_{Au} = 150$  nm for unpatterned Py nanowire and Py nanowire of Type I. The inset shows the respective velocities. (Fluctuations in the displacement-time relation for the patterned wire are too small to see clearly.) (d) and (e) Snapshot images of internal structures of the moving DWs at  $u = 200$  m/s in an unpatterned Py nanowire (d) and in a Py nanowire of Type I (e). The arrows indicate the DW position before movement.

contour plots, leading to some discontinuities in the contours. For all  $l_{Py}$ ,  $\langle v \rangle$  in the patterned wire initially increased with  $u$  to reach a maximum value  $\langle v \rangle_{Max}$  of 600–650 m/s, similar to the  $\langle v \rangle_{Max}$  for an unpatterned Py nanowire. As the Au pad spacing decreased,  $\langle v \rangle_{Max}$  increased slightly, and the value of  $u$  (i.e.,  $u_{Max}$ ) corresponding to  $\langle v \rangle_{Max}$  increased, showing that the pads enabled higher  $u$  to be applied prior to breakdown. A second maximum in  $\langle v \rangle$ ,  $\langle v \rangle_{Max2}$  corresponded

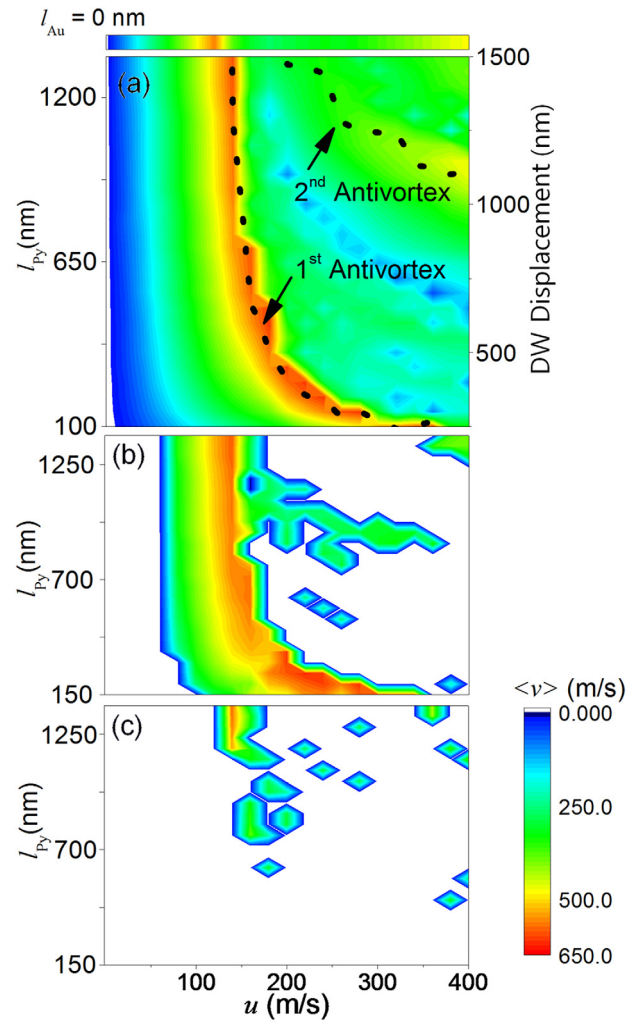


FIG. 3. (Color online) (a) Average DW velocity  $\langle v \rangle$  as a function of  $u$  and  $l_{Py}$  at  $l_{Au} = 150$  nm in the Type I structure. At each  $l_{Py}$  ranging from 150 nm to 1350 nm, the  $\langle v \rangle$  was calculated from the time taken by the DW to move 4  $\mu$ m. The top panel shows the DW velocity in an unpatterned wire. Overlaid on the data for the patterned wire is the DW displacement for the first and second introductions of an antivortex core in an unpatterned wire. (b)  $\langle v \rangle$  as a function of  $u$  for the Type II geometry where the initial DW core magnetization is parallel to the Oersted field. (c)  $\langle v \rangle$  as a function of  $u$  for the Type II geometry where the initial DW core magnetization is antiparallel to the Oersted field.

to the combination of  $u$  and  $l_{Py}$  that suppressed every second transformation of the DW. The dashed lines superposed on Fig. 3(a) show the DW displacement (taken as the distance the DW moved before  $v$  reached its peak value) at which the first and second antivortex cores were introduced for an unpatterned Py nanowire. This indicates that the enhancement in  $\langle v \rangle$  is greatest when the Au pads are placed at the positions where the antivortex core is introduced into the Py nanowire during DW motion.

Varying  $l_{Au}$  from 100 to 300 nm for fixed  $l_{Py}$  (not shown) indicated that  $\langle v \rangle$  was higher when  $l_{Au}$  was smaller. However, in order to prevent Walker breakdown  $l_{Au}$  must be long enough to allow the antivortex core that formed in the  $l_{Py}$  regions to return to the edge of the wire and be eliminated; therefore, there is an optimum  $l_{Au}$  to maximize  $\langle v \rangle$ . For a given  $u$ , when  $l_{Py}$  was longer, the antivortex core moved further across the wire before reaching the Au-covered region, so a longer  $l_{Au}$  was required to remove the

core and suppress breakdown. The maximum average velocity  $\langle v \rangle_{\text{Max}}$  was obtained when  $l_{\text{Py}} \sim 2l_{\text{Au}}$ , but  $\langle v \rangle_{\text{Max}}$  decreased slowly as  $l_{\text{Py}}$  and  $l_{\text{Au}}$  increased.

These results show that the Au pads can delay the onset of breakdown, allowing higher current to flow before breakdown initiates, but the DW velocity at which breakdown occurs is similar to the velocity in a wire without pads. For  $u$  smaller than the value that causes breakdown in an unpatterned wire, the DW will travel faster in the unpatterned wire, but for higher  $u$ , the DW travels faster in the heterostructured wire.

We now consider the effect of the Oersted field by examining Type II structures. The Oersted field is oriented in plane transverse to the wire length with a small out-of-plane component increasing towards the wire edges. In Type II geometry, the maximum Oersted field inside the capped region of the Py nanowire increased linearly as a function of  $u$ , reaching 250 Oe transverse to the wire at  $u = 300$  m/s.

Fig. 3(b) shows a map analogous to Fig. 3(a) for the Type II structure in which  $\langle v \rangle$  is plotted as a function of  $l_{\text{Py}}$  and  $u$  for  $l_{\text{Au}} = 100$  nm, for the case when the magnetization at the center of the DW was parallel to the Oersted field. The map shows some similarities to Fig. 3(a), but outside the band of high  $\langle v \rangle$  the velocity is zero over much of the parameter space. At low  $u$  and  $l_{\text{Py}}$  (e.g., the region  $u < 80$  m/s in Fig. 3(b)), the DW became trapped *under* the Au pad by the field, and  $\langle v \rangle = 0$ . The maximum  $\langle v \rangle$  in the band of non-zero velocity corresponded to the situation where an antivortex had been introduced in the DW just before it reached the pad, and the DW was then able to traverse the region of Py under the pad. At higher  $u$  and/or  $l_{\text{Py}}$ , the DW had transformed into a transverse wall with its center magnetization antiparallel to the Oersted field before it reached the Au pad, and it became trapped at the *leading* edge of the pad, giving another region of  $\langle v \rangle = 0$ . (An increase in  $\beta$  promoted the evolution of the antivortex and lowered the value of  $l_{\text{Py}}$  corresponding to these situations.)

In the case of antiparallel orientation between the center of the DW and the Oersted field, Fig. 3(c), the DW became pinned at the leading edge of the Au pad and  $\langle v \rangle$  was zero over most of the parameter space. A magnetic field antiparallel to the magnetization at the center of the DW is known to lower the DW velocity<sup>28–31</sup> and this, combined with the drop in  $u$  caused by current shunting, prevented the DW from passing under the pad for most combinations of  $l_{\text{Py}}$  and  $u$ . A non-zero  $\langle v \rangle$  was obtained when an antivortex nucleated shortly before the DW encountered the pad.

The different responses of the DW to an Oersted field parallel or antiparallel to the magnetization at the center of the DW allows the structure to act as a chirality filter for DWs, by selecting geometrical parameters and  $u$  values that pin one DW chirality while allowing the other DW chirality to be transmitted. This has an analogy to the cross-shaped chirality filter of Ref. 15 demonstrated for field-driven DW propagation, but in our case the design of the Au pads allows simultaneous control over both the Oersted field and the spin current in the magnetic wire for current-driven DW motion, while having no effect on field-driven DW motion.

The chirality filter effect can be generalized to other values of Oersted field and  $u$  by allowing the Au thickness to

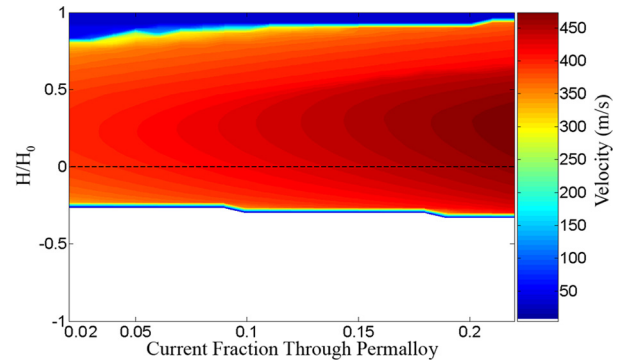


FIG. 4. (Color online)  $\langle v \rangle$  as a function of the Oersted field  $H_0$  and fraction of current shunted for a wire with Au pads in which the thickness of the Au on each side of the wire is varied. Positive  $H_0$  indicates Oersted field parallel to the DW core. The asymmetry between positive and negative  $H_0$  provides a chirality filter over a wide range of Oersted field and spin current.

vary on each side of the Py wire. When all the Au is on one side of the Py, the Oersted field takes a maximum value,  $H_0$ , for a given  $u$ , as exemplified by Type II, whereas when the Au is of equal thickness on each side of the Py, the Oersted field is zero, as in Type I. Therefore, values of Oersted field in the range  $\pm H_0$  can be obtained by varying the thickness distribution of the Au. Additionally, the amount of current shunted by the Au and the magnitude of  $H_0$  can be changed by changing the total Au thickness.

Fig. 4 shows the DW velocity for the case where  $u = 160$  m/s in the uncapped Py and  $l_{\text{Py}} = l_{\text{Au}} = 100$  nm for the full range of Oersted fields and current shunt fractions that can be obtained by independently varying the Au thickness between 0 and 10 nm on each side of the Py. The maximum Oersted field is  $H_0 = 130$  Oe for this geometry when  $u = 160$  m/s. There is a robust range of conditions in which a DW with core parallel to the Oersted field is transmitted, whereas a DW of opposite chirality is blocked (white region, with zero velocity). This result allows for a straightforward design of a chirality filter for current-driven DW motion simply by placing a thin conductive strip on the magnetic wire to shunt the current, without affecting the coercivity of the wire or the response of the DW to a magnetic field along the wire.

These computational results show that Walker breakdown of a current-driven transverse DW can be delayed to higher values of spin current by the placement of conductive shunt pads which locally reduce the spin current density with no effect on field-driven DW motion. The Oersted field present in asymmetrically shunted wires provides a DW chirality filtering effect. Suppression of oscillatory transformations of DWs is advantageous for DW devices such as racetrack memories or logic, and the interplay between the geometry of the shunt pads, the current density, and the DW velocity enables control over DW motion which can be implemented experimentally.

The support of the NRI INDEX Program, the Singapore-MIT Alliance, and the National Science Foundation is gratefully acknowledged. This work was also supported by the National Research Foundation of Korea Grant funded by the Korean Government (No. NRF-2009-352-D00127).

- <sup>1</sup>S. S. P. Parkin, M. Hayashi, and L. Thomas, *Science* **320**, 190 (2008).
- <sup>2</sup>M. Hayashi, L. Thomas, R. Moriya, C. Rettner, and S. S. P. Parkin, *Science* **320**, 209 (2008).
- <sup>3</sup>D. A. Allwood, G. Xiong, M. D. Cooke, C. C. Faulkner, D. Atkinson, N. Vernier, and R. P. Cowburn, *Science* **296**, 2003 (2002).
- <sup>4</sup>D. A. Allwood, G. Xiong, C. C. Faulkner, D. Atkinson, D. Petit, and R. P. Cowburn, *Science* **309**, 1688 (2005).
- <sup>5</sup>N. L. Schryer and L. R. Walker, *J. Appl. Phys.* **45**, 5406 (1974).
- <sup>6</sup>M. Hayashi, L. Thomas, C. Rettner, R. Moriya, and S. S. P. Parkin, *Nat. Phys.* **3**, 21 (2007).
- <sup>7</sup>G. S. D. Beach, C. Nistor, C. Knutson, M. Tsoi, and J. L. Erskine, *Nature Mater.* **4**, 741 (2005).
- <sup>8</sup>G. S. D. Beach, M. Tsoi, and J. L. Erskine, *J. Magn. Magn. Mater.* **320**, 1272 (2008).
- <sup>9</sup>Y. Nakatani, A. Thiaville, and J. Miltat, *Nature Mater.* **2**, 521 (2003).
- <sup>10</sup>J.-Y. Lee, K.-S. Lee, and S.-K. Kim, *Appl. Phys. Lett.* **91**, 122513 (2007).
- <sup>11</sup>K. Weerts, W. Van Roy, G. Borghs, and L. Lagae, *Appl. Phys. Lett.* **96**, 062502 (2010).
- <sup>12</sup>M. Yan, A. Kákay, S. Gliga, and R. Hertel, *Phys. Rev. Lett.* **104**, 057201 (2010).
- <sup>13</sup>A. Kunz and S. C. Reiff, *Appl. Phys. Lett.* **93**, 082503 (2008).
- <sup>14</sup>E. R. Lewis, D. Petit, L. O'Brien, A. Fernandez-Pacheco, J. Sampaio, A.-V. Jausovec, H. T. Zeng, D. E. Read, and R. P. Cowburn, *Nature Mater.* **9**, 980 (2010).
- <sup>15</sup>E. R. Lewis, D. Petit, A.-V. Jausovec, L. O'Brien, D. E. Read, H. T. Zeng, and R. P. Cowburn, *Phys. Rev. Lett.* **102**, 057209 (2009).
- <sup>16</sup>A. Thiaville, Y. Nakatani, J. Miltat, and Y. Suzuki, *Europhys. Lett.* **69**, 990 (2005).
- <sup>17</sup>S. Zhang and Z. Li, *Phys. Rev. Lett.* **93**, 127204 (2004).
- <sup>18</sup>L. Heyne, M. Kläui, D. Backes, T. A. Moore, S. Krzyk, U. Rüdiger, L. J. Heyderman, A. Fraile Rodríguez, F. Nolting, T. O. Mentis *et al.*, *Phys. Rev. Lett.* **100**, 066603 (2008).
- <sup>19</sup>A. Vanhaverbeke, A. Bischof, and R. Allenspach, *Phys. Rev. Lett.* **101**, 107202 (2008).
- <sup>20</sup>L. Thomas, M. Hayashi, X. Jiang, R. Moriya, C. Rettner, and S. S. P. Parkin, *Nature* **443**, 197 (2006).
- <sup>21</sup>M. Hayashi, L. Thomas, Ya. B. Bazaliy, C. Rettner, R. Moriya, X. Jiang, and S. S. P. Parkin, *Phys. Rev. Lett.* **96**, 197207 (2006).
- <sup>22</sup>R. Moriya, L. Thomas, M. Hayashi, Ya. B. Bazaliy, C. Rettner, and S. S. P. Parkin, *Nat. Phys.* **4**, 368 (2008).
- <sup>23</sup>O. Boule, J. Kimling, P. Warnicke, M. Kläui, U. Rüdiger, G. Malinowski, H. J. M. Swagten, B. Koopmans, C. Ulysse, and G. Faini, *Phys. Rev. Lett.* **101**, 216601 (2008).
- <sup>24</sup>M. Hayashi, L. Thomas, C. Rettner, R. Moriya, Y. B. Bazaliy, and S. S. P. Parkin, *Phys. Rev. Lett.* **98**, 037204 (2007).
- <sup>25</sup>M. J. Donahue and D. G. Porter, OOMMF User's Guide, version 1.0., Interagency Report NISTIR 6376, National Institute of Standards and Technology, Gaithersburg, MD, 1999.
- <sup>26</sup>K. L. Chopra, L. C. Bobb, and M. H. Francombe, *J. Appl. Phys.* **34**, 1699 (1963).
- <sup>27</sup>L. K. Bogart and D. Atkinson, *Appl. Phys. Lett.* **94**, 042511 (2009).
- <sup>28</sup>S. Glathe, I. Berkov, T. Mikolajick, and R. Mattheis, *Appl. Phys. Lett.* **93**, 162505 (2008).
- <sup>29</sup>J. Lu and X. R. Wang, *J. Appl. Phys.* **107**, 083915 (2010).
- <sup>30</sup>A. Kunz and S. C. Reiff, *J. Appl. Phys.* **103**, 07D903 (2008).
- <sup>31</sup>M. T. Bryan, T. Schrefl, D. Atkinson, and D. A. Allwood, *J. Appl. Phys.* **103**, 073906 (2008).